Int. J. Therm. Sci. (2000) 39, 332–353

S1290-0729(00)00222-2/FLA

Numerical predictions of two-dimensional conduction, convection, and radiation heat transfer. II. Validation

Daniel R. Rousse [a]*, Guillaume Gautier [a], Jean-Francois Sacadura [b]

[a] *Département de génie mécanique, Université Laval, Cité Universitaire, Québec, Canada G1K 7P4*

[b] *Centre de Thermique de Lyon (CETHIL)–INSA de Lyon, Bâtiment 404, 69621 Villeurbanne cedex, France*

(Received 4 March 1999, accepted 26 August 1999)

Abstract — This paper presents several test problems that were used to validate the formulation and implementation of a CVFEM for combined-mode heat transfer in participating media. The objective here is to demonstrate that the proposed CVFEM can be used to solve combined modes of heat transfer in media that emit, absorb, and scatter radiant energy in regularly- and irregularly-shaped geometries. The paper first assesses briefly the CVFEM for the solution of convection–diffusion problems, then attention is focused on radiative heat transfer problems. Finally, several combined mode problems are investigated. Results show that the proposed method adequately solves the governing equations (energy and RTE): as the solutions compare favorably with those obtained with other acknowledged methods or with analytical solutions, when available. The proposed CVFEM could, however, be improved to broaden its scope of application and enhance its numerical efficiency. In a near future, the method will be combined with a code already established for fluid flow calculations. © 2000 Éditions scientifiques et médicales Elsevier SAS

control volume finite elements method / discrete ordinates / combined modes heat transfer / two-dimensional / validation

Résumé — **Prédictions numériques du transfert par conduction, convection, et rayonnement thermiques. II. Validation.** Cet article présente quelques cas tests ayant été utilisés afin de valider la formulation et l'implantation d'une Méthode d'Éléments Finis basée sur des Volumes de Contrôle (MEFVC) pour la résolution du transfert thermique combiné dans des milieux semi-transparents. L'objectif consiste ici à démontrer que la méthode proposée peut être utilisée pour résoudre des problèmes de thermique couplés dans des milieux qui émettent, absorbent et diffusent le rayonnement en géométries irrégulières ou non. L'article confirme tout d'abord rapidement que les problèmes de convection–diffusion peuvent être résolus adéquatement. Par la suite, des problèmes de rayonnement thermique pur sont étudiés. Enfin, quelques problèmes où interviennent convection, diffusion et rayonnement sont présentés. Les résultats présentés permettent d'affirmer que la méthode proposée fournit des solutions adéquates au modèle mathématique (équations d'énergie et de transfert radiatif) employé pour décrire le phénomène d'intérêt. Toutefois des prolongements et améliorations peuvent être envisagés pour élargir les domaines d'application de la méthode et accroître son efficacité numérique. Dans un avenir rapproché cette méthode sera combinée à un code établi permettant les prédictions des écoulements fluides. © 2000 Éditions scientifiques et médicales Elsevier SAS

méthode éléments finis volumes de contrôle / ordonnées discrètes / modes couplés de transfert thermique / bi-dimensionnel / validation

Nomenclature

A	coefficient of the discretization equation, surface area	
Bo	Boltzmann number	
c_p	medium specific heat	$J \cdot kg^{-1} \cdot K^{-1}$
e	emissive power	$W \cdot m^{-2}$
g	incident radiant energy	$W \cdot m^{-2}$
i	radiative intensity	$W \cdot m^{-2} \cdot sr^{-1}$
$\vec{J}$	dimensionless flux (conductive, convective or radiative)	
k	medium conductivity	$W \cdot m^{-1} \cdot K^{-1}$
L	characteristic length	m
N	Stark number, number of panels	
$\vec{n}$	unit vector normal to a surface	
p	control volume surface (panel)	
Pe	Peclet number	
$\vec{q}$	heat flux	$W \cdot m^{-2}$
q'''	internal heat generation	$W \cdot m^{-3}$
Q_l^m	impinging dimensionless radiative flux	

* Correspondence and reprints.
Daniel.Rousse@gmc.ulaval.ca

$Q_{\mathrm{B}}^{\mathrm{in}}$	total incoming dimensionless radiative flux	
r	reference point for RTE integration	
s	spatial position	m
S_ϕ	rate of volumetric generation of ϕ	
S_I	source of radiative intensity	
T	temperature	K
$\vec{u}$	velocity	$\mathrm{m{\cdot}s^{-1}}$
V	volume	$\mathrm{m^3}$

Greek symbols

β	extinction coefficient	$\mathrm{m^{-1}}$
ε	normalized nodal percentage error	
$\tilde{\varepsilon}$	normalized residual	
ϵ	emissivity of a surface	
γ	albedo for single scattering	
κ	absorption coefficient	$\mathrm{m^{-1}}$
$\tilde{\omega}$	solid angle	sr
$\vec{\Omega}$	direction of propagation	
ϕ	dependent variable	
Φ	phase function for scattering	
μ, η, ξ	direction cosines of $\vec{\Omega}$	
ρ	medium density	$\mathrm{kg{\cdot}m^{-3}}$
σ	scattering coefficient	$\mathrm{m^{-1}}$
$\tilde{\sigma}$	Stefan–Boltzmann constant, 5.67051E−8	$\mathrm{W{\cdot}m^{-2}{\cdot}K^{-4}}$
τ	optical depth	
τ_0	optical thickness	
$\vec{\omega}$	angular velocity	

Subscripts

$*$	reference quantity
b	black body
B	boundary
l	control volume surface (panel)
m	discrete direction
P	node of reference
r, r	radiation, or reference point

Superscripts

$*$	evaluated at a preceeding step of an iterative procedure
$\vec{\ }$	vectorial quantity
$'$	incoming direction
–	bulk value
$\sim$	a modified quantity
C	convection term
D	diffusion term

1. INTRODUCTION

In a companion paper [1], the formulation of a Control-Volume Finite Element Method (CVFEM) for the solution of two-dimensional, combined-mode heat transfer problems in gray participating media is presented. Some of the capabilities of this CVFEM are demonstrated in this paper by its application to several different test problems involving steady-state combined conduction, convection, and radiation in emitting, absorbing and isotropically scattering media. The assesment of the method is carried out in three steps: (1) convection–diffusion problems; (2) radiation heat transfer problems; and (3) combined-modes problems. The following problems were considered in this first phase of validation:

- Convection–diffusion problems: (1) radial conduction in a rotating hollow cylinder; (2) heat transfer in a radial flow between concentric cylinders; and (3) heat transfer in a recirculating flow within a square enclosure.
- Radiation heat-transfer problems: (1) gray scattering media in a rectangular enclosure; (2) gray absorbing media in a rectangular enclosure; (3) gray absorbing media in a trapezoidal enclosure; (4) gray absorbing, emitting, and scattering media in an L-shaped enclosure; and (5) gray absorbing media in a curved enclosure.
- Combined-modes problems: (1) conduction–radiation in a rectangular enclosure; (2) conduction–convection–radiation in a rectangular enclosure; and (3) conduction–convection–radiation in a divergent channel.

These test problems were chosen as they: (1) cover several commonly encountered features of two-dimensional, combined-mode heat transfer in gray gases; (2) allow for an evaluation of the key ideas put forth in the development of the CVFEM; (3) provide a means of determining whether, or not, the proposed CVFEM and its computer implementation are capable of accurately solving the mathematical model used in the formulation [1]; (4) demonstrate the possibility to apply the proposed CVFEM in irregularly-shaped geometries.

For each problem, steady-state conditions, homogeneous, constant thermophysical and radiative properties, and radiatively participating gray media are considered [1]. No relaxation was used in the computations. The iterations were terminated when the absolute value of the residual on the incident radiation G, from one iteration to the next, met a prescribed condition $\tilde{\varepsilon}$. In test problems considered here $\tilde{\varepsilon} = 10^{-6}$ was found to be satisfactory: it yielded solutions that were essentially insensitive to further reductions in $\tilde{\varepsilon}$.

Structured-grids, with nodes arranged along straight or curved lines, were employed for all investigations presented here. Various ways of forming triangular elements

from quadrilaterals were investigated. With regard to angular discretization, the angular discretization was always customized so as to match the physical boundaries of the domain with $\phi - \theta$ azimuthal discretization, except in regular geometries for which standard equal weight S_n discretization were used. Results are presented in terms of dimensionless variables and a nodal percentage error. This error is denoted by ε, and calculated as follows:

$$\varepsilon = \frac{|\phi_{\text{ref}} - \phi_{\text{num}}|}{\phi_{\text{scale}}} \cdot 100 \qquad (1)$$

where ϕ_{num} is the quantity of interest as computed with the proposed CVFEMs, ϕ_{ref} is the corresponding quantity as obtained from an analytical solution, an accepted approximate numerical solution, or a nodally *exact* numerical solution; and ϕ_{scale} is a suitable scale for ϕ.

The formulations were implemented on a Pentium II 266 MHz with 256 MB RAM, using the MSDev FORTRAN 90 compiler.

The complete formulation, objectives, computational details, and results of each of the example problems are described in the remainder of this paper. The last section presents the general conclusions of the study.

2. CONVECTION–DIFFUSION PROBLEMS

For all convection–diffusion test cases investigated, the values of the dimensionless temperature were specified using either nodally "exact" numerical solutions [2] or analytical solutions, when available. The internal values of temperature were set to zero at the beginning of the iterative process. The problems were solved for several values of the Peclet number in the range $0.01 < Pe < 10\,000$. The low values represent conduction-dominated problems, while high values of Pe indicate convection-dominated processes. Conditions for $Pe = 10\,000$ are not physically possible as the flow would be turbulent for $Pr = 1$. The convection–diffusion problems permit a comparison of the Skew Positive Coefficient Upwind (SPCU) scheme and FLow-Oriented (FLO) scheme, and provide confidence in the formulation and implementation of the proposed procedure to solve the energy equation.

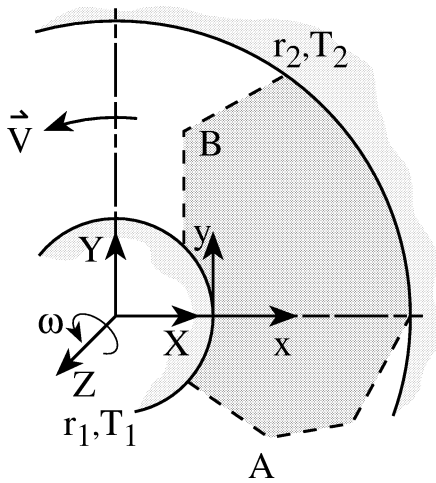

Figure 1. Heat conduction in a rotating hollow cylinder: problem schematic.

2.1. Heat conduction in a rotating hollow cylinder

2.1.1. Problem statement

This problem [3] is schematically depicted in *figure 1*. A hollow cylinder filled with fluid with its axis coincident with the Z axis of a Cartesian coordinate system (X, Y, Z), is considered to rotate as a solid body about the Z axis with a constant angular velocity, $\vec{\omega} = \omega\vec{k}$. The inner surface is maintained at a constant temperature T_1, while the outer surface is maintained at a constant temperature T_2.

Considering steady-state conditions, constant thermophysical properties of the material, and heat generation, q''', this problem is one of pure radial conduction in the radial direction, $\vec{r}$. But, with reference to the *fixed* two-dimensional calculation domain depicted by dashed lines in *figure 1*, the problem appears two-dimensional when it is observed from the fixed Cartesian system (x, y), located at r_1. As a result, the material within the fixed domain has a steady velocity given by

$$\vec{V} = u\vec{i} + v\vec{j} = \vec{\omega} \times \vec{r} \quad \text{with } u = -\omega y \text{ and } v = \omega x \qquad (2)$$

2.1.2. Numerical details and results

For Peclet numbers in the range $0.01 \leq Pe \leq 10\,000$, and for several values of the constant source term, Q''', the exact one-dimensional solution was used to specify the reference values of temperature over the two-dimensional calculation domain. Results for the maximum value of ε (see equation (1)), produced by FLO

TABLE I
Heat conduction in a rotating hollow cylinder. Variation of ε_{max} with Peclet number for a 11×11 grid and two different discretizations.

	Constant source term, Q'''					
	0		1.0		10.0	
Pe	FLO	SPCU	FLO	SPCU	FLO	SPCU
0.01	1.51E−2	1.51E−2	2.64E−2	2.48E−2	6.88E−2	5.96E−2
	1.51E−2	1.60E−2	2.64E−2	2.73E−2	6.88E−2	6.88E−2
1.00	1.51E−2	1.93E−2	2.64E−2	1.78E−1	6.88E−2	1.04E+0
	1.49E−2	1.16E−1	2.64E−2	1.13E−1	6.77E−2	8.57E−2
100.00	1.89E+0	3.53E+0	1.35E−1	3.29E+0	2.77E+1	1.22E+1
	3.18E−1	4.18E+0	2.609E−1	3.99E+0	1.65E+0	1.08E+1
10 000.00	5.76E+0	4.28E+0	6.94E+0	4.72E+0	2.77E+1	1.45E+1
	5.13E−1	5.15E+0	3.53E−1	5.19E+0	2.66E+0	1.16E+1

and SPCU schemes, were obtained and solution accuracy with grid refinement was investigated. Results are presented in *table I* for two types of discretizations (top and bottom values) and for a coarse 11×11 grid to show the maximum discrepancies between the schemes. The solution with such a grid is relatively sensitive to the orientation and shape of the elements. Here, results are presented for the worst case to support the following discussion. Errors reported are high as the reference temperature on the external cylinder was taken as the scale value, ϕ_{scale}, in equation (1).

In conduction-dominated situations, $Pe < 1$, both the SPCU and the FLO schemes produce results of similar accuracy. For small Peclet numbers, the influence of the different approximations of convection embedded in the interpolation schemes is minimal, as the contributions to the coefficients of the algebraic discretized equations by convection transport terms are small compared to those due to diffusion. However, the FLO scheme, even for such a low Peclet number, was found to produce small negative coefficients in the discretized equations with the two distorted meshes employed.

For $Pe > 1$, important negative coefficients were produced with the FLO scheme with distorted grids. The shape of the elements, with such grids, influences the relative magnitude of the negative coefficients. *Table I* shows that the errors differ by an order of magnitude for the two discretizations employed (that is with quadrilaterals divided from top-left to bottom-right or from top-right to bottom-left, respectively). Nevertheless, it was possible to obtain convergent solutions with the FLO scheme for the proposed three values of constant source term, Q'''. In *table I* the error with the FLO scheme reaches the order of 10 %. In other test cases (results are not shown here), involving a regular grid and a square domain, the relative magnitude of the negative coefficients was significantly less, and the error, ε_{max}, was always below 1 %.

For $Pe > 1$ and $Q''' = 10$, the SPCU scheme is found to require a finer spatial discretization than the relatively coarse 11×11: the error for both discretizations is greater than 10 %. One of the difficulties with this problem, when $Q''' \neq 0$, is the presence of important cross-flow temperature gradients close to radius $r = (r_1 + r_2)/2$, where the dimensionless temperature is substantially larger than one. Since the fluid flows in the counter-clockwise direction, the error introduced in the calculation of the dimensionless temperature at a location downstream of point *A* in *figure 1*, is propagated and amplified until the fluid crosses the opposite boundary: the maximum numerical error, ε_{max}, is found in the immediate vicinity of point *B*. More grid points in the cross-flow direction close to $r = (r_1 + r_2)/2$ in *figure 1* should be used to reduce smearing or false diffusion [4].

2.2. Heat transfer in a radial flow between concentric cylinders

2.2.1. Problem statement

One of the characteristics of the previous test problem is that the exact solution is independent of the Peclet number. Thus, following the discussions of LeDain and Baliga [5], it may not be a very strict and true test of

the proposed method's response to *Pe*. To overcome this drawback, the following test problem was employed.

A schematic representation of this test problem is shown in *figure 2*. The temperature boundary conditions on the cylinders are the following: $T = T_1$ at $r = r_1$, and $T = T_2$ at $r = r_2$. In this problem, the cylinders are at rest and convection–diffusion transport of energy is in the radial direction from the inner to the outer cylinder.

Considering steady-state conditions, constant thermophysical properties of the fluid, and heat generation, q''', this problem is governed by the one-dimensional radial convection–diffusion equation. Here, to satisfy continuity requirements, the fluid velocity, u_R, has to be inversely proportional to the radius ($u_R \propto 1/r$). With respect to the *fixed* two-dimensional regular calculation domain denoted by dashed lines in *figure 2*, the one-dimensional problem in the radial direction becomes two-dimensional when it is observed from the fixed Cartesian system (x, y). The material flowing in the radial direction crosses the fixed two-dimensional domain boundaries, and the fluid velocity is given by

$$\vec{V} = u\vec{\imath} + v\vec{\jmath} = \frac{1}{r}\vec{e_R} \quad \text{with}$$
$$r\vec{e_R} = x\vec{\imath} + y\vec{\jmath}; \quad u = \frac{x}{r^2}; \quad v = \frac{y}{r^2} \tag{3}$$

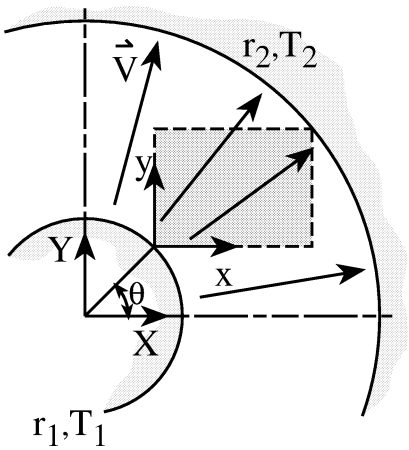

Figure 2. Heat transfer in a radial flow: problem schematic.

2.2.2. Numerical details and results

The exact analytical solution (and a one-dimensional numerical method) were used as a means to validate the results produced by the CVFEM. *Table II* shows results for the same grid and source terms as previously. In the computation of $\varepsilon_{\max}$, the dimensionless temperature on the external cylinder was also taken as the scale value, ϕ_{scale}, in equation (1).

For no source term, $Q''' = 0$, it was found that for values of the Peclet number above one hundred, $Pe > 100$, the conditions at $r = r_1$ essentially prevail throughout the domain, until a very sharp variation takes place close to $r = r_2$ in order to match the imposed condition at this boundary.

TABLE II
Heat transfer in a radial flow between concentric cylinders. Variation of $\varepsilon_{\max}$ with Peclet number for an 11×11 grid and two different discretizations.

	Source term, Q'''					
	0.0		1.0		10.0	
Pe	FLO	SPCU	FLO	SPCU	FLO	SPCU
0.01	5.56E−3	4.42E−3	5.60E−3	4.44E−3	5.97E−3	4.71E−3
	5.63E−3	5.66E−3	5.67E−3	5.66E−3	6.05E−3	5.90E−3
1.00	5.71E−4	3.01E−2	1.68E−4	1.46E−1	2.59E−3	6.62E−1
	3.73E−3	4.38E−2	7.98E−3	1.37E−2	2.57E−2	2.81E−1
10.00	1.13E−2	2.69E+0	4.80E−2	1.57E+0	7.49E−2	4.97E+0
	3.57E−2	1.72E+0	2.53E−2	5.72E−1	3.48E−2	2.49E+0
100.00	7.51E−1	2.11E+0	8.51E−1	1.18E+0	1.40E+0	1.37E+0
	5.64E−1	1.44E+0	1.09E+0	2.04E+0	1.14E+0	2.09E+0
10 000.00	–	–	2.15E+0	1.77E+0	2.15E+0	1.77E+0
	–	–	1.19E+1	2.89E+0	1.19E+1	2.89E+0

As long as the convection term is smaller or equal to the diffusion term, $Pe \leq 1$, for the source terms investigated here, both schemes provide solutions that are within 1 % of the reference solution even for a relatively coarse regular 11 × 11 grid. In simulations where $1 < Pe \leq 10$, the maximum error occurs in the region next to the outer cylinder, and the SPCU scheme predictions of the temperature distribution are significantly less accurate than those obtained with the FLO scheme. In convection-dominated situations, $Pe > 10\,000$, for all source terms, the maximum error is found in the immediate vicinity of $r = r_2$, and the negative coefficients in the discretized equations produced by the FLO scheme gained in importance: the SPCU scheme produced better predictions than the FLO scheme.

Here again the results selected for presentation in *table II* are those which show the maximum discrepancies between the two schemes and reference solution. For the 11 × 11 grid, the type (shape) of elements greatly influenced the results. However, as the grid was refined, the discrepancies between the results obtained with different elements diminished, and the solution accuracy improved for both schemes.

2.3. Heat transfer in a recirculating flow within a square enclosure

2.3.1. Problem statement

The problem, for which an analytical solution can be constructed [6], is illustrated schematically in *figure 3*. In this figure, a 2 × 2 square enclosure is depicted, with the origin of a Cartesian coordinate system (x, y) located at its center.

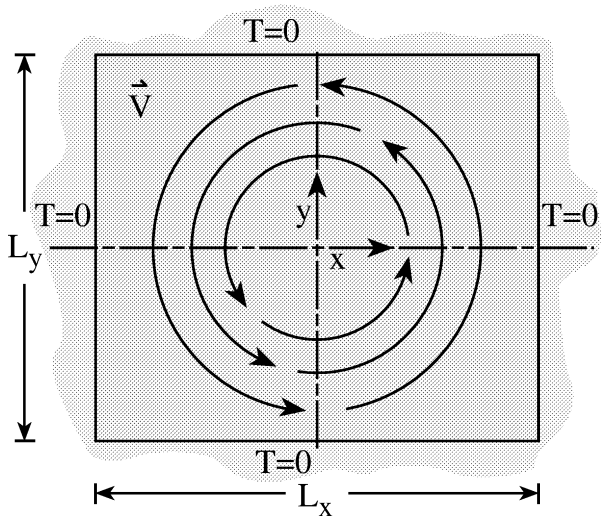

Figure 3. Heat transfer in a recirculating flow within a square enclosure: problem schematic.

The recirculating velocity field is specified via:

$$u = \left(2x^2 - x^4 - 1\right)\left[y - y^3\right]$$
$$v = -\left(2y^2 - y^4 - 1\right)\left[x - x^3\right] \tag{4}$$

and the following temperature field is proposed as a solution:

$$T = \left(1 - x^2\right)\left(1 - y^2\right) \tag{5}$$

When the expressions for velocity and temperature are incorporated in the energy equation, the following expression for the source term is required to satisfy energy conservation:

$$Q''' = 2\left\{\left(1 - x^2\right) + \left(1 - y^2\right)\right\} \tag{6}$$

In this problem, the temperature, the velocity, and the source term vary across the domain. As a consequence, it tests the combined effects of velocity, temperature, and source term distributions on the accuracy of the solution method.

2.3.2. Numerical details and results

Table III indicates that for both schemes, grid refinement leads to accuracy improvement. The FLO scheme accurately solves the equations at high *Pe*, even on grids as coarse as the 11 × 11 grid: the error was 1.53 % and 2.44 % for the two discretizations used, respectively. However, for the same grid, the SPCU scheme was as far as 14 % off the expected solution for the temperature distribution. This error was nevertheless cut in half (6.93 %) when the other discretization was used. The error was reduced to 2.52 % when the number of grid nodes per direction was nearly quadrupled (41 × 41). Moreover, this maximum error obtained for $Pe = 10\,000$ further decreased, by a factor 2 (1.34 %), for a 81 × 81 grid (not presented in *table III*).

The results showed that in conduction-dominated situations, both schemes provide excellent accuracy. At intermediate and high Peclet number, the FLO scheme predictions are significantly more accurate than those obtained with the SPCU scheme. This test case does not present the sharp temperature gradients found in the previous two problems. As a result the FLO scheme produced positive coefficients only, and the first-order SPCU scheme always provided adequate accuracy.

TABLE III
Heat transfer in a recirculating flow within a square enclosure. Variation of ε_{max} with Peclet number for several regular grids and two different discretizations.

	Discretization					
	11 × 11		21 × 21		41 × 41	
Pe	FLO	SPCU	FLO	SPCU	FLO	SPCU
0.01	2.86E−5	7.86E−4	7.52E−6	3.96E−4	2.03E−6	1.98E−4
	3.65E−5	4.76E−4	9.61E−6	2.41E−4	2.53E−6	1.21E−4
1.00	2.98E−5	7.83E−2	7.58E−4	3.95E−2	1.91E−4	1.97E−2
	3.70E−5	4.71E−2	9.52E−4	2.41E−2	2.41E−4	1.21E−2
10.00	3.05E−2	7.48E−1	7.92E−3	3.79E−1	2.00E−3	1.92E−1
	3.97E−2	4.12E−1	1.00E−2	2.15E−1	2.56E−3	1.11E−1
100.00	2.20E−1	4.27E+0	5.81E−2	2.29E+0	1.47E−2	1.20E+0
	2.90E−1	1.36E+0	7.12E−2	7.30E−1	1.78E−2	3.80E−1
10 000.00	1.53E+0	1.40E+1	6.38E−1	8.55E+0	1.76E−1	4.85E+0
	2.44E+0	6.93E+0	5.64E−1	4.73E+0	1.47E−1	2.52E+0

2.4. Conclusion regarding convection–diffusion

2.4.1. SPCU scheme

The SPCU scheme always gave better results when the longest side of the triangular element was nearly aligned with the average local flow field. For such an element, the interpolation distances in the direction of the largest velocity variations are shorter, and this results in a better approximation of the velocity distribution. Also, in the evaluation of the interpolated value of the dependent variable at an integration point, a panel and a nodal value are involved with such an element, in contrast to a single nodal value with a short-sided element.

In the implementation of the SPCU scheme, when the analytical velocity distribution was available, the mass flow rate across the control-volume surfaces (panels) was calculated using: (1) linear interpolation of velocity; (2) Simpson's rule or Gaussian quadrature integration of velocity on a panel, with integration point values specified via the analytical profile; and (3) exact integration of the velocity profile. The exact integration respects mass conservation precisely—but this condition is not guaranteed by the other types of integration. However, in the test cases considered here, it should be mentioned that no significant gains in accuracy were observed using exact integration. This is an interesting result because the analytical velocity field is not available in general, and because Euler integration of ϕ combined with the linear velocity interpolation, is simple and inexpensive. The linear interpolation of velocity within each element is thus recommended for the approximation of mass flow rates involved in the SPCU scheme.

2.4.2. FLO scheme

Generally, whenever the FLO scheme produced convergent solutions, its results were more accurate than the results of the SPCU scheme. The errors in the FLO scheme predictions for problems with irregular geometries were higher than those for problems with regular domains. Similar results were also obtained by Saabas [2]. When negative coefficients in the discretized equations are produced by the FLO scheme, but the magnitude of these negative coefficients is small, the predictions are generally very accurate for fine grids over the entire range of Peclet number tested. However, important negative coefficients can lead to solutions that are less accurate. Finally, convergence problems were encountered with the FLO scheme when the negative coefficients became significant at high values of Peclet number and/or with highly distorted grids. This was observed in preliminary tests, when very skewed elements were employed in the discretization of the highly-irregular calculation domains. Extrapolation, rather than interpolation, occurred in obtuse-angle triangular elements for high Peclet numbers, leading to negative coefficients in the algebraic discretization equations [7].

2.4.3. SPCU and FLO schemes

One of the reason for the differences between FLO- and SPCU-based solutions could be that the surface integration of the dependent variable in the FLO scheme is carried out using Simpson's rule [5], which is more accurate than the prevailing assumption used in Euler integrations involved with the SPCU scheme [1]. Moreover, the mass-weighted averages of ϕ involved in the SPCU scheme are intrinsically cruder approximations of the influence of the direction and the strength of the convective transport within an element, than that provided by the flow-oriented Peclet-number-based function used with the FLO scheme.

2.4.4. Concluding remarks

The present investigation suggests that: (1) flow-oriented *Pe*-based interpolation functions or similar should be used whenever converged solutions—with relatively small negative coefficients in the discretized equations, if any—can be obtained; (2) a combination of FLO and SPCU schemes is desirable to avoid computation of negative coefficients and still obtain high accuracy; or (3) modifications should be incorporated in the SPCU scheme to enhance its capabilities to approximate the influences of the direction and strength of the flow within an element. The effect of Peclet number and volumetric source terms could be explicitly included in the SPCU scheme used to provide algebraic approximations to the integrated convected flux terms in the governing energy equation. This enhanced scheme would still avoid the appearance of negative coefficients in the algebraic discretization equations.

The results obtained for the three test problems presented here demonstrated that the formulation and implementation of the proposed CVFEM have been carried out correctly. The interested reader should contact the corresponding author for more details.

3. RADIATION HEAT TRANSFER PROBLEMS

In this section, the issue of validation with respect to selected radiation heat transfer problems is presented.

In the notation for the dimensionless net radiant heat flux, $\vec{Q}_{\mathrm{r}}$, the vector and the subscript r are dropped for ease of presentation, whenever this does not lead to any misunderstanding. The term *net* is also omitted, as the definition of $\vec{Q}_{\mathrm{r}}$ accounts for radiation coming from all directions. Whenever a particular definition of radiant heat flux with respect to a surface is employed, the term *incoming* or *outgoing* will be specified.

For purely absorbing media the *exact* (reference) solution is calculated with

$$I_P = I_r\,\mathrm{e}^{-\tau} + I_{\mathrm{b}}\left(1 - \mathrm{e}^{-\tau}\right) \tag{7}$$

where I_r is the intensity at an upstream location along a discrete direction $\vec{\Omega}$, τ is the optical depth between r and P measured along $\vec{\Omega}$, and I_{b} is the blackbody intensity of the media. To obtain the net dimensionless flux, a numerical quadrature is used. Practically, a very fine angular discretization (*ndd* directions) is employed to compute the flux in order to minimize the error due to the quadrature approximation. The refinement is stopped when further increases in the number of directions does not yield a significant change in the solution.

The exponential and upwind schemes were used with the CVFEM.

3.1. Gray scattering media in a rectangular enclosure

3.1.1. Problem statement

In the enclosure depicted in *figure 4*, surface 4 is maintained at a constant temperature, T_4, and all other surfaces are assumed to be at a constant zero temperature, $T_1 = T_2 = T_3 = 0$. The medium is assumed to scatter radiation isotropically and does not absorb radiant energy ($\gamma = 1$). Results of the following investigators who

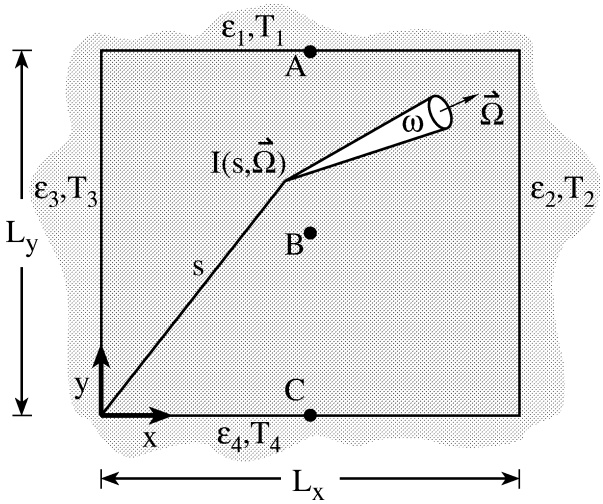

Figure 4. Heat transfer in a rectangular enclosure: problem schematic.

studied this problem were considered: Fiveland [8], Truelove [9], Modest [10], and Crosbie and Schrenker [11]. Their numerical solutions are used as references to check those obtained with the proposed CVFEM using the exponential and upwind schemes. T_4 is used as a reference temperature to obtain suitable nondimensional quantities. Here, $Q_r = q_r/\tilde{\sigma} T_4^4$ permits a direct comparison with the results presented in the above-listed references.

3.1.2. Numerical details and results

The effects of wall emissivities, aspect ratio, and optical thickness on the dimensionless radiant heat flux, Q_r, at the lower surface (wall 4), were investigated. For the results presented in this section, the spatial grid consisted of 400 uniform rectangular quadrilaterals, each divided into two triangular elements. An equal weight (EW) S_4 angular discretization was used.

In *figure 5(a)*, results are presented for square enclosures, $L_x/L_y = 1$, with unit optical thickness, $\tau_0 = 1$, having three different surface emissivities, ϵ, namely 1.0, 0.5, and 0.1. *Figure 5(a)* shows that the CVFEM solutions, for both schemes, are in good agreement with the reference solutions, and predictions for a black enclosure are somewhat more accurate than that obtained by Modest (diamonds) with a differential approximation (DA) [10]. As the emissivity decreases, the intensity leaving a boundary becomes increasingly dependent on the incident intensity on this boundary: as a result, the radiant heat flux at the hot wall becomes increasingly uniform and small with decreasing ϵ.

The effects of the variation of the enclosure aspect ratio, L_x/L_y, are presented in *figure 5(b)* for $\tau_0 = 1$ and $\epsilon = 1$. Here again, the results indicate that the CVFEM predictions are in good agreement with those of the zonal method (black diamonds) and Crosbie's method ($*$). Predictions for high aspect ratios are more accurate than those obtained by Modest [10].

The effect of the variation of the optical thickness, τ, is shown in *figure 5(c)* for $\epsilon = 1$ and $L_x/L_y = 1$: the results indicate once more that the proposed CVFEM can successfully predict radiant heat transfer in scattering media having medium ($\tau = 1$) to large ($\tau = 10$) optical thickness, as the predictions are in good agreement with the reference solutions.

CPU time and convergence rates were also investigated. For each scheme, it was found that the number of iterations required to obtain a converged solution increased with τ. It took approximately the same number of iterations with both schemes, with a slight advantage for the upwind scheme. However, the CPU time required

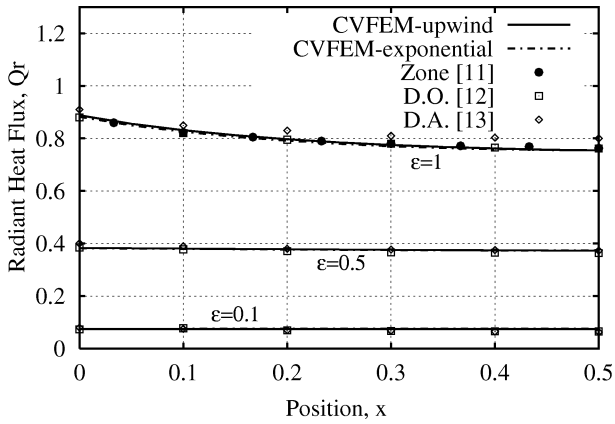

(a)

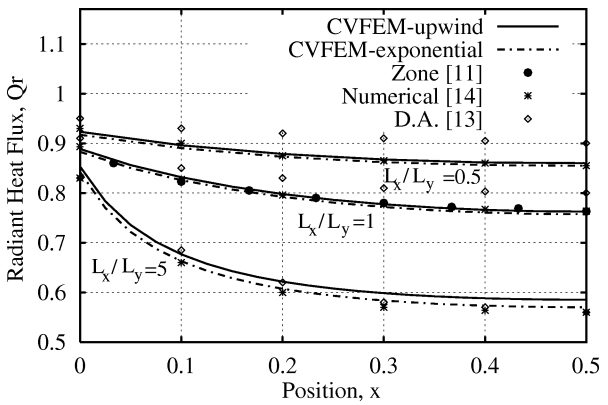

(b)

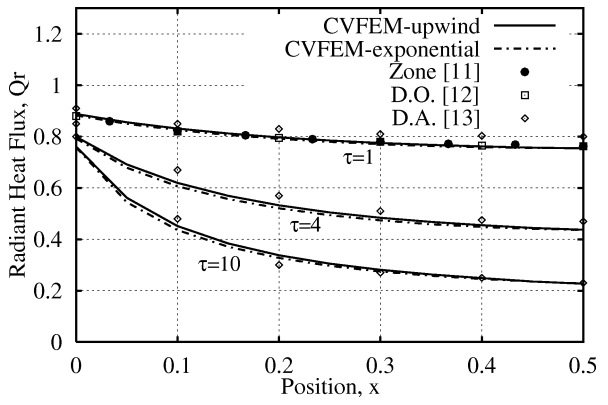

(c)

Figure 5. Distribution of dimensionless bottom surface radiant heat flux, Q_r, for scattering nonabsorbing media, $\gamma = 1$. (a) Effect of wall emissivity, ϵ, with $L_x/L_y = 1$ and $\tau_0 = 1$; (b) effect of aspect ratio, L_x/L_y, with $\epsilon = 1$ and $\tau_0 = 1$; and (c) effect of optical thickness, τ_0, with $L_x/L_y = 1$ and $\epsilon = 1$.

TABLE IV
Gray scattering media in a rectangular enclosure. Dimensionless radiant heat flux, Q_r, at the lower surface $\gamma = 1$, $\tau = 1$, $\epsilon = 1$, and $L_x/L_y = 1$.

Position	Exponential scheme				
x	11×11	21×21	41×41	81×81	[11]
0.0	0.8781	0.8824	0.8854	0.8872	0.8932
0.1	0.8262	0.8255	0.8244	0.8236	0.8273
0.2	0.7938	0.7920	0.7896	0.7888	0.7957
0.3	0.7741	0.7715	0.7688	0.7676	0.7773
0.4	0.7636	0.7604	0.7576	0.7564	0.7671
0.5	0.7608	0.7570	0.7540	0.7532	0.7636
Position	Upwind scheme				
x	11×11	21×21	41×41	81×81	[11]
0.0	0.8890	0.8886	0.8887	0.8890	0.8932
0.1	0.8266	0.8259	0.8252	0.8246	0.8273
0.2	0.7944	0.7934	0.7924	0.7920	0.7957
0.3	0.7759	0.7756	0.7748	0.7746	0.7773
0.4	0.7664	0.7655	0.7648	0.7644	0.7671
0.5	0.7626	0.7604	0.7590	0.7584	0.7636

per iteration for the upwind scheme was about 50 % of that of the exponential scheme. This is significant as the accuracy of both schemes is comparable.

Table IV indicates the numerical values of the dimensionless radiant heat flux on the lower surface for a unit optical thickness, unit aspect ratio, and black boundaries. The exact solution obtained by Crosbie and Schrenker [11] is also indicated for comparison. The spatial discretization specifications indicate the number of nodes along the x and y axes. When the incident radiant energy is considered, both schemes eventually yield the same solution with grid refinement. They both give about 0.5 % error, which is due to the EWS_4 angular discretization. For a given level of accuracy, the exponential scheme may require less nodes but about twice as much CPU time.

3.2. Gray absorbing media in a rectangular enclosure

3.2.1. Problem statement

In this test case, the proposed CVFEM is applied to a cold ($T_1 = T_2 = T_3 = T_4 = T_w = 0$) square enclosure filled with an absorbing medium ($\gamma = 0$) at constant temperature T_m. Here, the dimensionless radiant heat flux, Q_r, at any surface (because of symmetry) in *figure 4* is set equal to $q_r/(\tilde{\sigma} T_m^4)$.

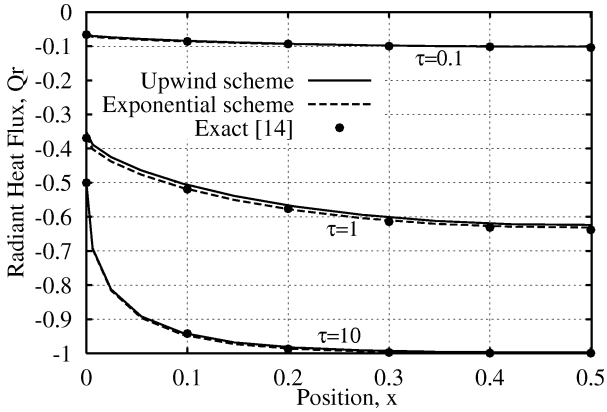

Figure 6. Distribution of dimensionless surface radiant heat flux, Q_r, for nonscattering absorbing media, $\gamma = 0$. Effect of optical thickness, τ, with $\epsilon = 1$, and $L_x/L_y = 1$.

3.2.2. Numerical details and results

Figure 6 illustrates the effect of the medium optical thickness, τ, on Q_r, for a square ($L_x/L_y = 1$) black walled ($\epsilon = 1$) enclosure. Results are presented for three different optical thicknesses, namely, 10.0, 1.0, and 0.1. Other tests were carried out but are not presented. *Figure 6* shows that the CVFEM solutions, with a EWS_4 discretization, are in good agreement with the exact numerical solutions, equation (7), for the upwind and exponential schemes. As τ increases, the intensity at any particular point becomes increasingly dependent on its immediate surroundings. For a boundary point P, the incoming intensity is then related to the intensity of a point in the medium very near P. As the boundary temperature is zero (zero outgoing radiant heat flux) and the medium temperature is T_m, for $\tau = 10$, Q_r is approximately unity. To capture the discontinuity of temperature at the boundary, mesh enrichment is needed in the vicinity of the walls. Otherwise, the CVFEM cannot accurately predict radiant heat fluxes at the walls, showing a 20 % error for $\tau = 10$.

3.3. Gray absorbing media in a trapezoidal enclosure

3.3.1. Problem statement

This test case involves the irregular quadrilateral enclosure depicted in *figure 7*. The enclosure is assumed to be filled with an absorbing but nonscattering medium ($\gamma = 0$) at constant temperature T_m, and the walls are assumed to be black and held at a constant zero temperature ($T_1 = T_2 = T_3 = T_4 = T_w = 0$). A FVM

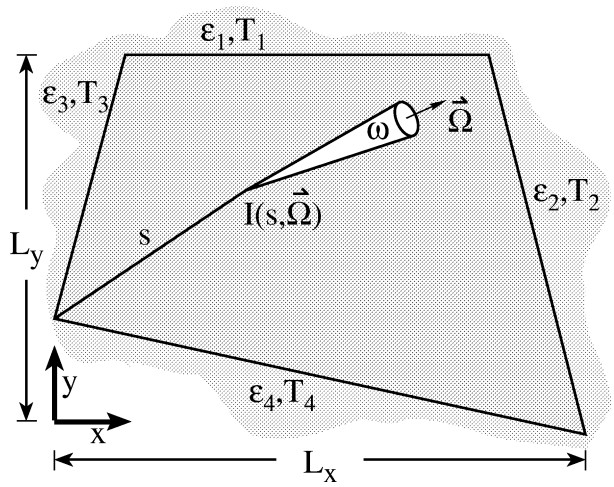

Figure 7. Gray media in a trapezoidal enclosure: problem schematic.

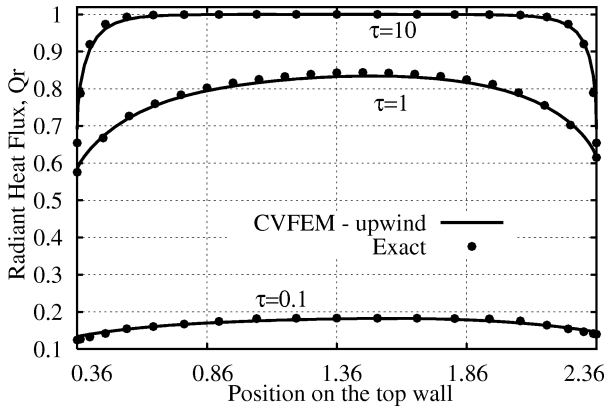

Figure 8. Dimensionless radiant heat flux on the top surface for absorbing media bounded by a black trapezoidal enclosure: Effect of optical thickness, τ.

solution for this problem has been proposed by Chui [12]. Since then, the problem has also been used by Chui and Raithby [13].

3.3.2. Numerical details and results

Figure 8 illustrates the effect of the optical thickness of the medium, τ, on the values of the dimensionless radiant heat flux, $Q_r = q_r/(4\sigma T_m^4)$, at the top wall. Here, a positive Q_r indicates a flux that leaves the enclosure. At the implementation level, the (x, y) coordinates of the four corners in the enclosure were: $(0.00, 0.90)$, $(0.36, 1.99)$, $(2.36, 1.99)$, and $(3.03, 0.00)$. A 41×41 spatial grid was required to match the exact solution faithfully. The azimuthal angular grid (16×4) was adjusted to make the projections of the edges of the solid angles match the orientations of the walls. That is to say the value of the azimuthal angle, ϕ, is first selected, then the values of θ are defined accordingly. In order to match the edges of the solid angles with the irregular quadrilateral domain boundaries, the azimuthal angular grid had to have a minimum of eight (8) solid angles in the ϕ (azimuthal) direction to span 2π in the (x, y) plane. For this type of geometry, the advantage of the analytical integration of $\vec{\Omega} \cdot \vec{n}$ over solid angles is clear. There is no need to compute the half range first moment and to select discrete directions associated with the solid angles.

The strict respect of the half range first moment is not critical for this particular problem because as long as all boundaries are black, the discrete representation of the boundary condition for intensity is independent of the angular discretization ($I_b = I_{Bb}$). However, the half-range first moment condition needs to be imposed on a boundary upon which the distribution of the radiant heat flux is desired. Indeed, the *incoming* radiant heat flux needs to be evaluated appropriately on this boundary.

CVFEM solutions for the radiant heat flux leaving the enclosure via the top wall, obtained with an angular discretization involving 8 directions, are presented for three different optical thicknesses, namely, $\tau = 10.0$, 1.0, and 0.1. *Figure 8* shows that the surface radiant heat fluxes predicted by the proposed CVFEM, with the upwind scheme, are in good agreement with the exact solutions. For thick media, the radiation from distant locations is mostly eliminated before it reaches a particular point: the radiative behavior at any point depends only on its immediate surroundings. This provides the incentive to employ a fine spatial mesh in the corners, as there are important changes in the radiant heat flux in these areas, especially for a thick medium. For the limit of a thin medium, $\tau = 0.1$, the surface radiant heat flux depends essentially on surface temperatures. As a result, the radiant heat flux at the top wall decreases with decreasing optical thickness because all surface temperatures are zero.

3.4. Gray media in an L-shaped enclosure

3.4.1. Problem statement

This test case involves the irregular-shaped enclosure shown in *figure 9*. The enclosure is assumed to be filled with an emitting, absorbing, and isotropically scattering medium at constant temperature T_m, and the walls are assumed to be black and held at a constant zero temperature ($T_w = 0$), except for the top wall where $T = T^*$. This is equivalent to assuming an outgoing radiant heat flux, Q_{in},

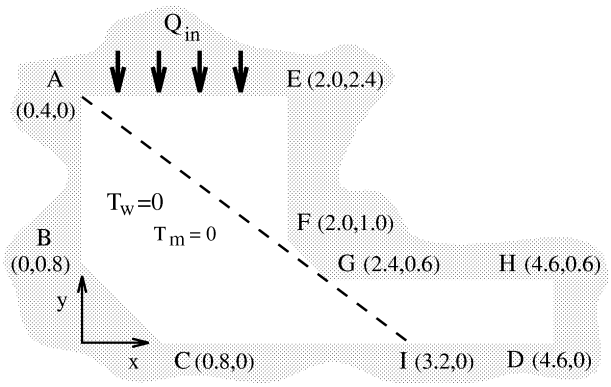

Figure 9. Gray media in an L-shaped two-dimensional enclosure: problem schematic.

on the top wall between point A and point E in *figure 9*. Here, the solutions proposed by Chui [12] using a FVM are used as references. Chai et al. [14, 15] also used this test case to assess their methods. $Q_{\text{in}} = 1$ for purposes of comparison with the solutions proposed in [12].

3.4.2. Numerical details and results

In a preliminary set of simulations, two situations were investigated: (1) the absorption coefficient, $\kappa = 0.01$, and the scattering coefficient, $\sigma = 1.00$, yielding $\gamma = 1/1.01$; and (2) the case of no scattering, $\sigma = 0$, with $\kappa = 0.01$. Grid refinement as well as optical thickness effects were investigated. The above-described furnace involves a particularly interesting feature because the non-orthogonal boundaries make a 45° angle with the (x, y) coordinate system shown in *figure 9*. Therefore, it is easy to employ a *boundary matching* angular discretization with at least 2 solid angles per quadrant of the (x, y) plane.

Figure 10 illustrates the dimensionless radiant heat flux, Q_{r}, at the *left-south* wall, identified by points A, B, C, and D in *figure 9*. In *figure 10(a)* the medium both scatters $\sigma = 1.00$ and absorbs $\kappa = 0.01$ radiant energy while in *figure 10(b)* the medium absorbs $\kappa = 0.01$ radiant energy, only. In [12], the investigator employed a relatively coarse 11×4 spatial grid and an angular discretization that involved 2 latitudes and 8 longitudes within an octant. For this test case, the first spatial computational domain employed with the proposed method consisted of 52 irregular quadrilaterals, each divided into two triangular elements, and the angular grid was constructed using 16 discrete directions, that is one latitude in the positive z direction and 4 discrete solid angles in each quadrant of the (x, y) plane. A finer grid involving 33×15 nodes and 64 directions, distributed on two latitudes, was also

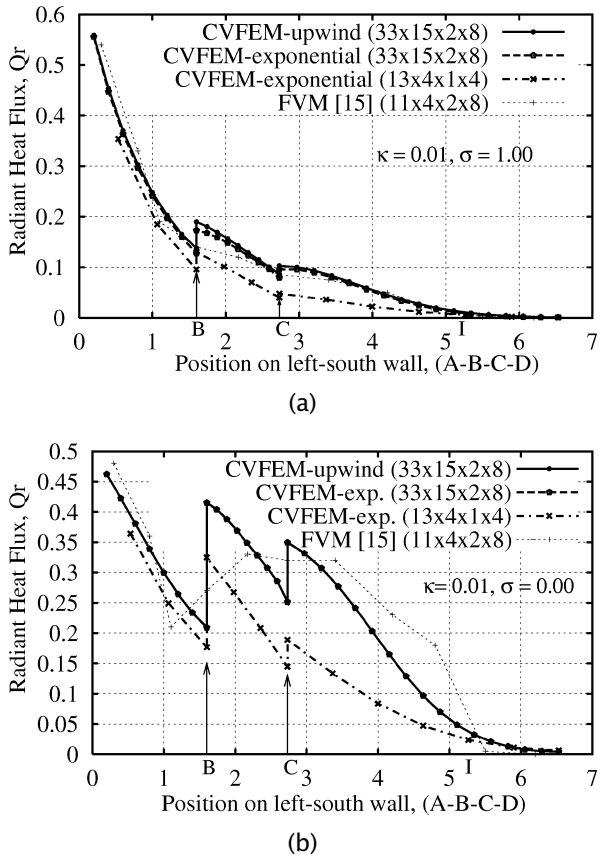

Figure 10. Distribution of dimensionless radiant heat flux, Q_{r}, on the left-south wall A-B-C-D for: (a) $\kappa = 0.01$, $\sigma = 1.0$; (b) $\kappa = 0.01$, $\sigma = 0.0$.

employed for direct comparison with Rousse [7]. In the notation indicated in the legend of the figures, the discretization is identified with 4 numbers: the first number refers to the number of grid nodes along the left-south wall (A-B-C-I-D) and right-north wall (E-F-G-H) of the enclosure depicted in *figure 9*; the second number is the number of grid nodes used on the top wall (A-E) and right wall (H-D); the third number refers to the number of latitudes employed with the azimuthal angular discretization; and the last number is the number of solid-angle projections in each quadrant of the (x, y) plane.

In *figure 10(a)*, the surface radiant heat flux, Q_{r}, along the left-south wall (A-B-C-I-D) decreases with the distance away from point A, measured between A and D, because radiation is attenuated by absorption and scattering as it travels away from the top (hot) wall. When there is no scattering, $\gamma = 0$ in *figure 10(b)*, the radiant heat flux impinging on a surface is very sensitive to the orientation of this surface with respect to the source Q_{in} (located on the top wall).

In *figure 10(b)* it can be observed that the FVM 11×4 fails to predict the two bumps, that correspond to locations B and C, in the surface radiant heat flux distribution. Chui's solution [12] indicates a plateau, while the 13×4 CVFEM solution shows the two peaks at point B and C. The CVFEM solution for a coarse grid is shown to be somewhat better than its corresponding FVM counterpart. This may be caused by the treatment of the boundary conditions and by the fact that in the CVFEM each quadrilateral is divided into two trianglular elements. This yields a finer discretization and hence a better approximation of the radiative fluxes across control volume surfaces.

The orientation of the wall changes at B and C, and this makes the left-south wall lie in a more direct line of sight from the source of radiation on the top wall (A-E). There should be discontinuities in the Q_r distribution at B and C for $\sigma = 0$. The tendency is well predicted by the relatively fine grid (33×15 nodes) combined with fine angular discretization involving 64 directions (2 latitudes and 8 projections per quadrant). To capture the flux discontinuities, grid points should be inserted close to points B and C. Beyond point C, along C-D, after the step B-C, the radiant heat flux is seen to decrease to zero, as some points (beyond point I) do not "see" the radiation source on the top wall A-E, and because there is no reflection and no emission from the boundaries. When scattering is present, *figure 10(a)*, the changes in the distribution of the radiant heat flux at point B and C are less pronounced because a direct line of sight to A-E is less important than in the case of no scattering in *figure 10(b)*. Chui's solution [12] and the coarse CVFEM solution indicate monotonic decrease of the radiant heat flux along the left-south wall, whereas the CVFEM solution obtained with a fine grid, which reproduces the physics more faithfully, shows the expected bumps at point B and C.

The radiant heat flux at the *right-north* wall (E-F-G-H in *figure 9*) was also computed (but not shown here) with more accuracy with the CVFEM than with the FVM of Chui [12]. The effect of angular and spatial discretization refinement and that of optical thickness were also investigated. Interested readers should consult the corresponding author for details.

3.5. Gray absorbing media in a curved enclosure

3.5.1. Problem statement

In this last test case for pure radiative heat transfer, a quarter of circle—with a rectangular region added on its top—was used as a test geometry. In *figure 11*, the curved wall is hot, $T_4 \neq 0$, and black, while all other walls are cold, $T_1 = T_2 = T_3 = 0$. The medium is cold and purely absorbing with $\kappa = 1$. The radius of the quarter of circle is equal to the length along the x-axis, $L_x = 1.0$, and $L_y = 1.5$. Chai et al. [14, 15] and Liu et al. [16] used this problem.

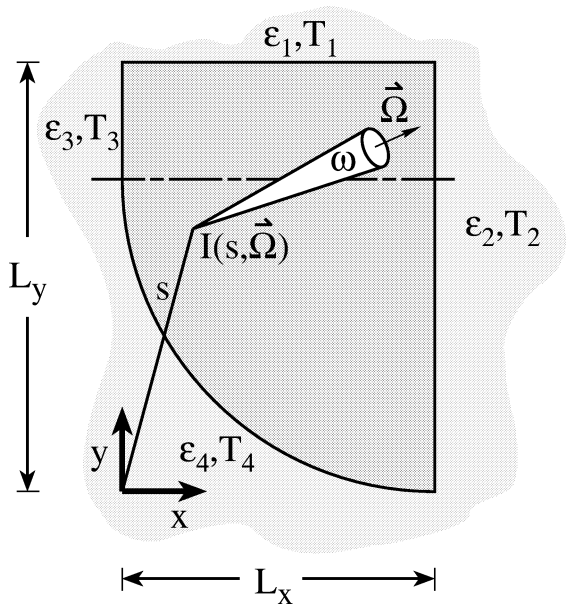

Figure 11. Gray media in a curved computational enclosure: problem schematic.

3.5.2. Numerical details and results

A 37×37 spatial grid and an azimuthal 20×4 grid in the ϕ and θ directions were employed with a progressive deployment of the spatial grid: there are more nodes in the immediate vicinity of the walls.

The predictions of the radiant heat flux on the right wall (wall 2) are illustrated in *figure 12*. It is shown that the CVFEM solution, using the upwind scheme, is in good agreement with that proposed by Chai et al. [15].

As the hot wall is curved, it is impossible on this surface to customise the angular discretization to have solid angle edges match the boundaries exactly for each boundary element. If the value of the incoming flux at this surface was the quantity of interest or if the curved wall was reflecting, a special treatment for the boundary conditions would be required. However, as this curved surface is black (no reflection), such a treatment is not necessary here: only the outgoing flux is needed on the curved boundary.

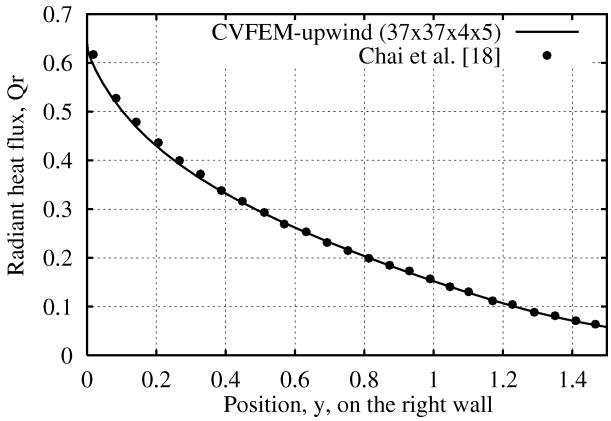

Figure 12. Distribution of dimensionless radiant heat flux, Q_r, on the right surface for absorbing media bounded by a black curved enclosure, $\beta = 1$.

3.6. Conclusion regarding radiation

The first two test cases permitted to compare the solution obtained with the CVFEM formulation with those of several investigators. The results indicate that the method was accurately formulated and implemented and that it can handle emission, absorption, and isotropic scattering in rectangular geometries. The third and fourth problems were introduced to show that irregular geometries can be handled with the proposed method. Finally, the fifth test case was proposed to demonstrate that the proposed CVFEM [1] is not restricted to applications with geometries where the angular discretization can be adjusted to make the solid angle edges coincide with the domain boundaries. In many practical situations, such an approach could lead to a high number of solid angles or, in other words, a high number of discrete dependent variables.

As boundaries were black for problem five and because the boundary upon which the flux is provided is straight, there was no need to implement a special treatment for the boundary conditions. However, in a more general case, provision should be made to account for solid angles that straddle boundaries. This particular approach requires care to ensure that the radiant energy is conserved at the gray-diffuse surface boundaries. The strict respect of energy conservation may not be that critical: for a sufficiently refined angular discretization, the very small solid angles straddling boundaries have the dot product of their associated direction with the normal to the boundary very small. This leads to a negligible overall effect. This, and other considerations that pertain to angular discretization in arbitrarily-shaped geometries, will be addressed in a subsequent study.

The upwind scheme is a low-order scheme that allows for a numerical redistribution of radiant energy in directions normal to the direction of propagation. Indeed, the upwind scheme always gave better results when the longest side of the triangular element was nearly aligned with the direction of propagation. For such situations, the prevailing assumption of a nodal intensity at a control volume face (panel) located downstream is more likely to describe the reality than when the panel is not in a direct line of sight from the node. The result is that when the flux and/or the incident radiant energy is calculated, there will be directions for which the mesh alignment is favorable and others not. Efforts will now be devoted to account for the direction of propagation at the spatial interpolation level.

Despite its drawbacks, the upwind (also called step) scheme was found to yield accuracy levels that were essentially similar, from an engineering point of view, to those obtained with the exponential scheme. The CPU time ratio for a given problem is also always in favor of the upwind scheme.

Isotropic scattering was considered in the test problems involved in this paper. However, provision has been made to account for anisotropic scattering and the prescription of a suitable phase function is at the discretion of the analyst.

The proposed CVFEM formulation [1] could also be improved by employing an implicit solution procedure building on ideas developed by Chui [12] in the context of pure radiative heat transfer with radiative equilibrium.

4. COMBINED MODES HEAT TRANSFER PROBLEMS

In this section, the solutions are obtained with the SPCU scheme when convection is taken into account and with the upwind and exponential schemes for the calculation of radiation heat transfer [1]. However, as the solutions obtained with the upwind and exponential schemes are very close to each other for all problems involved here, only those produced by using the upwind scheme are presented.

4.1. Conduction–radiation in a rectangular enclosure

4.1.1. Problem statement

In the enclosure depicted in *figure 4*, $T_4 = T_w$ and all other surfaces are assumed to be at a constant tem-

perature, $T = 0.5T_w$. The lower corners of the enclosure are considered to be at $T = 0.75T_w$. The medium is assumed to be continuous, and only conductive and radiative transfer occur in the enclosure. The medium is further assumed to absorb and emit radiation, but not scatter radiant energy, $\gamma = 0$. The optical thickness is assumed to be $\tau_0 = 1.0$, and $L_x/L_y = 1$. In the nondimensional formulation, the side of this square enclosure is of unit length. This problem has been investigated by Razzaque et al. [17]. In that paper, the authors employed the Galerkin finite element method, with isoparametric, biquadratic, quadrilateral elements, and an iterative solution technique.

4.1.2. Numerical details and results

The effects of the conduction to radiation parameter, the Stark number, $N = \beta k/(4\tilde{\sigma}T_w^3)$, on the vertical centerline (line *A-B-C* in *figure 4*) temperature, T/T_w, and on the dimensionless *total* heat flux, $Q = q/(\tilde{\sigma}T_w^4)$, at the lower surface, were investigated. The results are presented in *figure 13*. The CVFEM solutions were obtained with a EWS_4 angular discretization, combined with a 41×41 uniform spatial grid with both the upwind and exponenetial schemes for the calculation of radiation.

In *figure 13(a)*, the distribution of dimensionless temperature, T/T_w, along the centerline for three different values of N is presented. A CVFEM solution is also given for the case of no radiation, $N = \infty$. This figure shows that the CVFEM solutions (with the upwind scheme) for the centerline temperature profile are in very good agreement with those presented by Razzaque et al. [17]. When the Stark number is unity, the temperature profile is not greatly affected by radiation when compared to the case of pure conduction. This suggests that the magnitude of the ratio of the radiant heat transfer to the conduction heat transfer should be at least unity to require a radiation heat transfer calculation ($N \leq 1$). It can be seen that with decreasing N, the source term in the energy equation becomes more and more important in the upper region of the domain. In *figure 13(b)*, results are presented for $0 \leq x \leq 0.5$, as the total heat flux distribution is symmetric with respect to point C on the bottom wall. The CVFEM predictions for the total heat flux, Q, at the bottom wall are also in good agreement with those proposed in [17]. In this figure, the peak near the corner (low x position) for $N = 1$ is due to the fact that lower corner nodes are assigned a lower temperature than the rest of the bottom wall nodes. For this case, the solution is grid sensitive and the comparison remains meaningful as long as general trends are discussed. The sharper curve close to corner for $N = 1$ may be explained by the coarse discretization and the interpolation function used. Discrete variations imply strong influences on the fisrt-order upwind scheme.

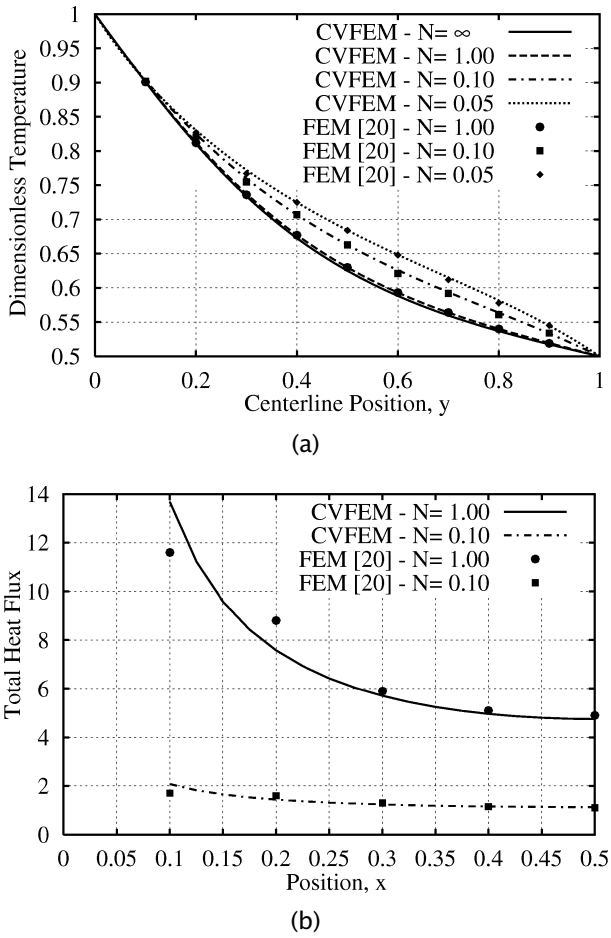

Figure 13. Conduction–radiation in a square black ($\epsilon = 1$) enclosure with absorbing media, $\gamma = 0$, and different values of the Stark number, N: (a) centerline temperature distribution; (b) total heat flux, Q, on the bottom surface.

4.2. Conduction–convection–radiation in a rectangular enclosure

4.2.1. Problem statement

Combined convection–diffusion–radiation is considered in a fully-developed laminar flow within the geometry depicted in *figure 4*. This geometry is considered to be a straight horizontal gray channel ($L_x > L_y$) in which the media participate in the radiative heat transfer. The temperature is set to $T_1 = T_4 = T_w$ on the top and bottom surfaces, and these surfaces are considered

to be opaque, parallel to each other, gray-diffuse, and to have constant emissivities, ϵ. The inlet and outlet sections of the channel are assumed to be imaginary porous black surfaces, through which the media flow without restrictions. The inlet temperature profile is first assumed to be zero, $T_3 = 0$, and the temperature gradient at the outlet surface is set to zero. Fully-developed Poiseuille flow is considered with a velocity given by $u(x, y) = 6\bar{u}[(y/L_y) - (y/L_y)^2]$ where L_y is the channel width and $\bar{u}$ the average velocity. For purpose of comparison, attention was focused on a location of the fully-developed heat transfer region where the centerline dimensionless temperature is $T = 0.5T_w$. This location is located at a distance $L_y/2$ in *figure 4*, but not necessarily located at the center of the channel, $L_x/2$. The results obtained using the proposed CVFEM [1] are compared with those obtained by Viskanta [18], who considered fully-developed heat transfer in emitting and absorbing media, $\gamma = 0$. In [18], the axial temperature gradient, $\partial T/\partial x$ was replaced by

$$\left(\frac{T_w - T}{T_w - \overline{T}}\right)\frac{d\overline{T}}{dx}$$

and conduction as well as radiation in the axial direction were neglected.

4.2.2. Numerical details and results

For this test case, many grid nodes were used along the axial direction to capture the location, in the fully-developed heat transfer region, where the centerline temperature is 0.5. The number of grid nodes employed in the cross-flow direction was adjusted to obtain triangles with aspect ratios near one. An EWS_4 angular discretization was employed. The inlet boundary condition for T_3 had to be adjusted, after preliminary tests, so as to obtain fully-developed heat transfer within a reasonable channel length. The results are presented for a relative optical depth measured along segment A-B in *figure 4*.

The dimensionless temperature profile along a vertical segment A-B, in *figure 4*, is presented for several values of the conduction–radiation parameter, N, in *figure 14(a)*. In this figure, results are presented for a unit optical thickness, $\tau = \beta L_y = 1$, in the cross flow direction. The effect of the optical thickness variations on the local radiant heat flux $\vec{Q}_r$ along A-B is presented in *figure 14(b)* for $N = 0.01$. In this figure, radiant heat flux profiles are shown for $\tau = 1.0$ and for $\tau = 0.1$.

The value of the Nusselt number (7.54 based on $D_h = 2L_y$) for pure convection–diffusion was first calculated. Then, radiation heat transfer was combined with convection and conduction. As N decreases, the temperature field departs more and more from that of pure convection–diffusion, $N = \infty$. In [18], the investigator found that the temperature gradient at the wall decreased with decreasing N. But Viskanta [18] stated that this was an error introduced by the approximation embedded within his numerical method. In [18], the author uses a three terms Taylor series expansion (Barbier's method) to evaluate the integral terms of the integro-differential governing equation. The temperature gradient at the wall is then in error. Nevertheless, the shape of the curve is generally adequate [18].

The CVFEM proposes a temperature gradient that is relatively unaffected by the Stark number, N. An examination of the results suggests that the proposed two-dimensional CVFEM [1] adequately predicts temperature

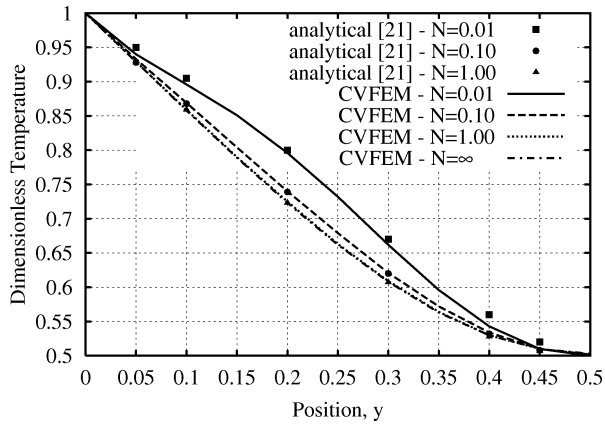

(a)

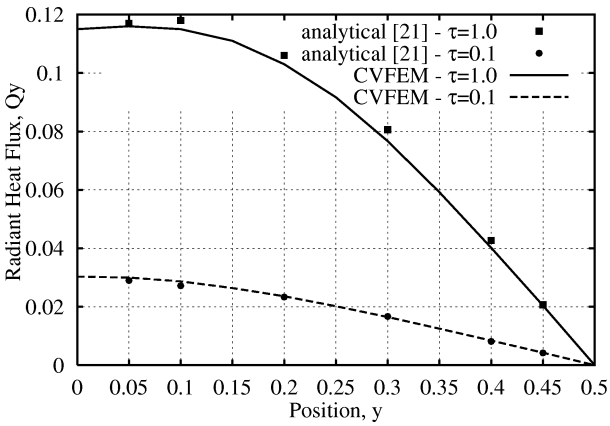

(b)

Figure 14. Conduction–convection–radiation in a gray channel with absorbing media: (a) effect of Stark number, N, on temperature; and (b) effect of optical thickness, τ, on the local radiant heat flux.

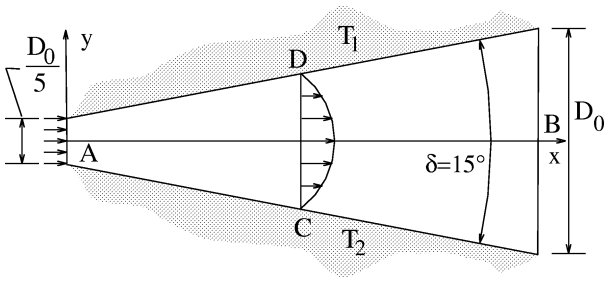

Figure 15. Gray media in a divergent channel: problem schematic.

and heat fluxes, when it is applied to this convection–diffusion–radiation problem in a regular geometry.

4.3. Conduction–convection–radiation in a divergent channel

4.3.1. Problem statement

This last two-dimensional test case involves an irregularly-shaped quadrilateral enclosure having the shape of a divergent channel. This geometry is depicted in *figure 15*. The top and bottom walls of this channel are maintained at uniform temperature T_1 and T_2, respectively. These two infinitely wide black plates, with an angle $\delta = 15°$, are separated by a distance D_0 at the channel exit. It is assumed that the velocity profile down the channel is fully developed, laminar flow, given by

$$u(x, y) = \frac{3}{2}\bar{u}_x\left[1 - 4\left(\frac{y}{D_x}\right)^2\right]$$

where $\bar{u}_x = (D_0/D_x)\bar{u}_L$, $\bar{u}_L$ is the average outlet velocity, and D_x is the channel width at x. The inlet and outlet sections of the divergent channel are assumed to be imaginary porous black surfaces, through which the media flow without restrictions. There is no heat generation, $Q''' = 0$, in the calculation domain, and the normal temperature gradients at the entrance and exit boundaries are set equal to zero. The media flowing along the channel are assumed to emit, absorb, and isotropically scatter radiant energy.

This problem was suggested by Chung and Kim [19] in a paper in which the authors used the Galerkin Finite Element Method (FEM) with a total of 72 linear two-dimensional isoparametric elements with 91 nodes. Although the overall mass conservation is preserved using the proposed u-velocity profile, continuity requirements are not satisfied everywhere in the domain. In [19], the authors did not specify any velocity profile in the y-direction, while in this work it is assumed that the cross-section velocity profile is given by

$$v(x, y) = \frac{3}{2}\bar{u}_x\left\{\left[1 - 4\left(\frac{y}{D_x}\right)^2\right]\frac{y}{D_x}\frac{\mathrm{d}D_x}{\mathrm{d}x}\right\} \quad \text{where}$$

$$\frac{\mathrm{d}D_x}{\mathrm{d}x} = \frac{4}{5}\frac{D_L}{L}$$

The oulet mean velocity, $\bar{u}_L$, and the outlet channel width, D_L, are used as reference velocity and length, respectively, in the specification of the velocity profiles. T_4 is assumed to be the reference temperature and $T_1 = T_4/5$.

4.3.2. Numerical details and results

72 quadrilaterals each divided into two triangular elements were first used, that is 13 grid nodes along the axial direction and 7 grid nodes in the cross-flow direction. This relatively coarse grid was employed to permit a more interesting comparison with the results presented in [19]. It was also found to yield sufficient accuracy except in the entrance region, when compared with a finer grid (results not shown). The SPCU scheme was used in the approximation of the convective flux, and inflow and outflow boundary conditions were imposed at the inlet and outlet, respectively. As the velocity profiles are expressed as functions of x and y, the evaluation of the mass flux at the control-volume faces (panels) was carried out with a second order accurate Simpson's rule integration. An azimuthal angular discretization about the z-axis was used with a single ξ latitude, and 12 solid angles, having 7.5° projections in the (x, y) plane, per octant. With reference to *figure 15*, the results are presented in terms of the dimensionless temperature along the centerline axial section, A-B, and the middle cross-section, C-D. Investigations were carried out for selected values of the Stark number, N, optical thickness, τ, Peclet number, Pe, and scattering albedo, γ. The Prandtl number, Pr, was one for all simulations. Results for the upwind scheme used in the interpolation for the radiative flux are reported.

In *figures 16* and *17*, results are presented for several Peclet numbers, $Pe = \rho c_p \bar{u}_L L/k$, a unit optical thickness, $\tau = \beta L = 1$, and for a Stark number $N = k\beta/(4\tilde{\sigma}T_2^3) = 0.001$.

Figure 16 presents results for a purely scattering medium, $\gamma = 1$. In this case, as the divergence of the radiative flux vector is zero, the source term in the energy equation is zero and the solution is that for pure

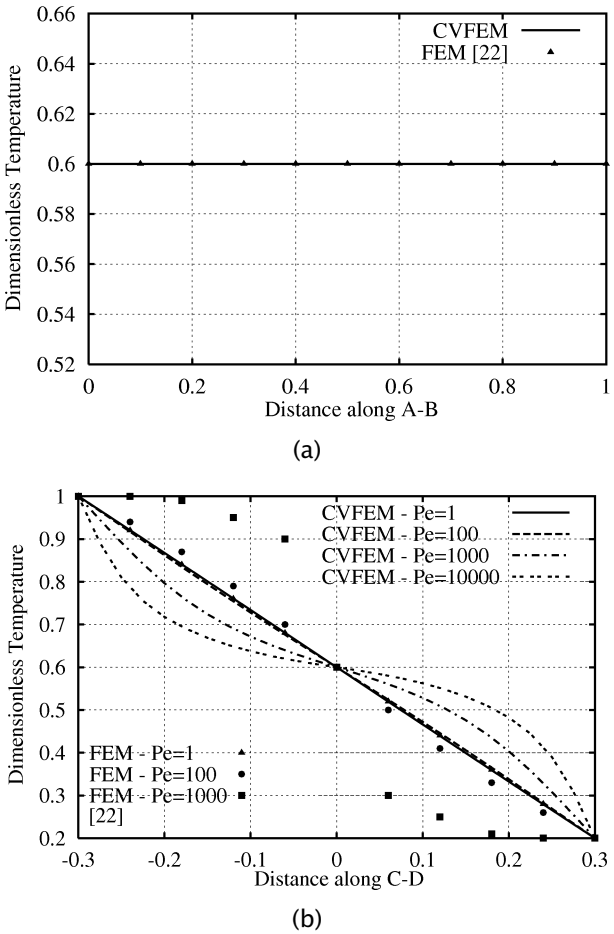

Figure 16. Conduction–convection–radiation in a divergent channel. Effect of Peclet number, *Pe*, on: (a) centerline temperature; (b) cross-flow temperature at $x = L_x/2$. $\gamma = 1$, $\tau = 1$, $N = 0.001$.

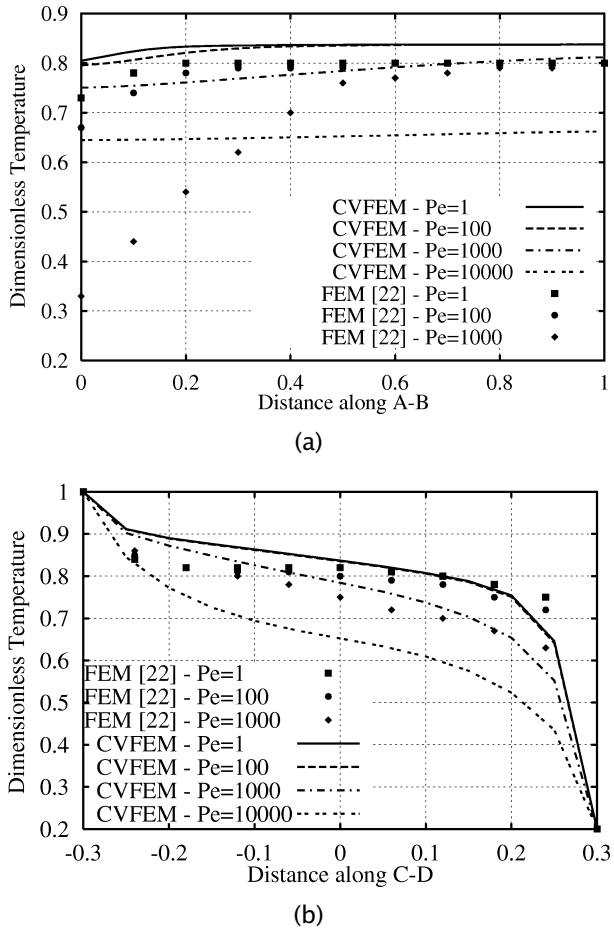

Figure 17. Conduction–convection–radiation in a divergent channel. Effect of Peclet number, *Pe*, on: (a) centerline temperature; (b) cross-flow temperature at $x = L/2$. $\gamma = 0$, $\tau = 1$, $N = 0.001$.

convection–diffusion. Hence, the temperature profile at the axial section, *A-B*, is not affected by the variations of the optical thickness, τ, the Stark number, N, and the Peclet number, *Pe*: a straight line is shown in *figure 16(a)*. However, in *figure 16(b)*, it will be noticed that as convection increases with respect to conduction, the heat transfer at the boundaries also increases: the CVFEM solution for the cross-section *C-D* indicates strong temperature gradients in the vicinity of the walls for high *Pe*. It is surprising to see that Chung and Kim [19] observed the inverse phenomenon for a purely scattering medium.

Figure 17 shows results for a purely absorbing medium, $\gamma = 0$. In this case, the divergence of the radiative flux at a point, $\vec{\nabla} \cdot \vec{Q}_r$, is negative except at the hot boundary. As a result, a positive source term is present in the energy equation and the temperature profile is raised above that obtained for a purely scattering medium. The CVFEM solutions for the axial temperature profile at *A-B* are not very dependent on the Peclet number until $Pe = 1\,000$ (see *figure 17(a)*). For $Pe < 1\,000$, the dimensionless temperature T/T_4 reaches about 0.8 very rapidly for $\tau = 1$. When $Pe = 1\,000$, $N = 0.001$, and $\tau = 1$; the Boltzmann number, *Bo*, is unity: thus, convection becomes as important as radiation and the effect of the source term in the energy equation becomes relatively less important than for $Pe < 1\,000$. As a result, the axial temperature profiles obtained for $Pe \geq 1\,000$ tend to approach that of a purely scattering medium because convection dominates radiation for such values of *Pe*. For $Pe = 1\,000$, Chung and Kim [19], obtained temperatures—in the vicinity of the channel inlet—that are below 0.6, as if there were a heat sink due to radiation in this area.

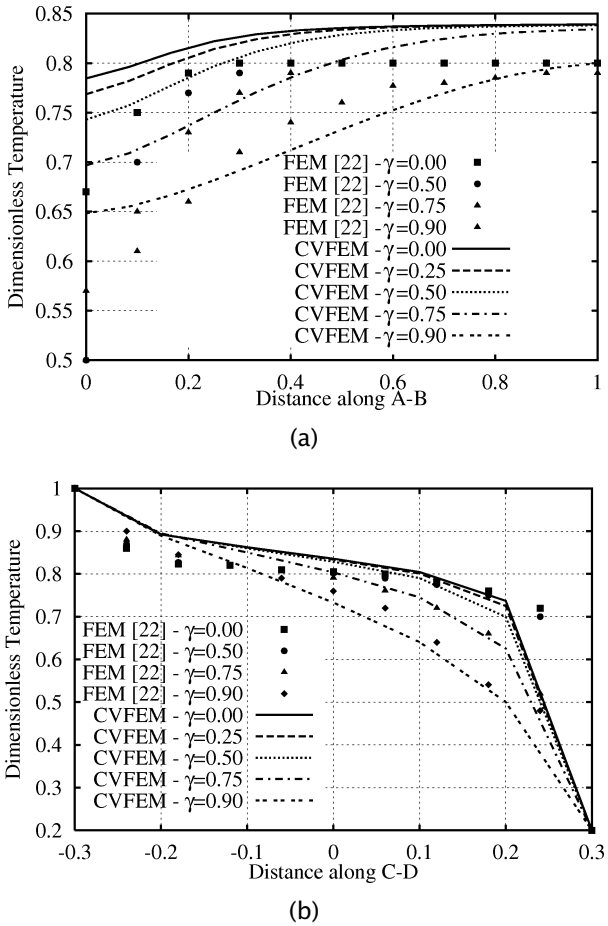

Figure 18. Conduction–convection–radiation in a divergent channel. Effect of scattering albedo, γ, on: (a) centerline temperature; (b) cross-flow temperature at $x = L/2$. $Pe = 100$, $\tau = 1$, $N = 0.001$.

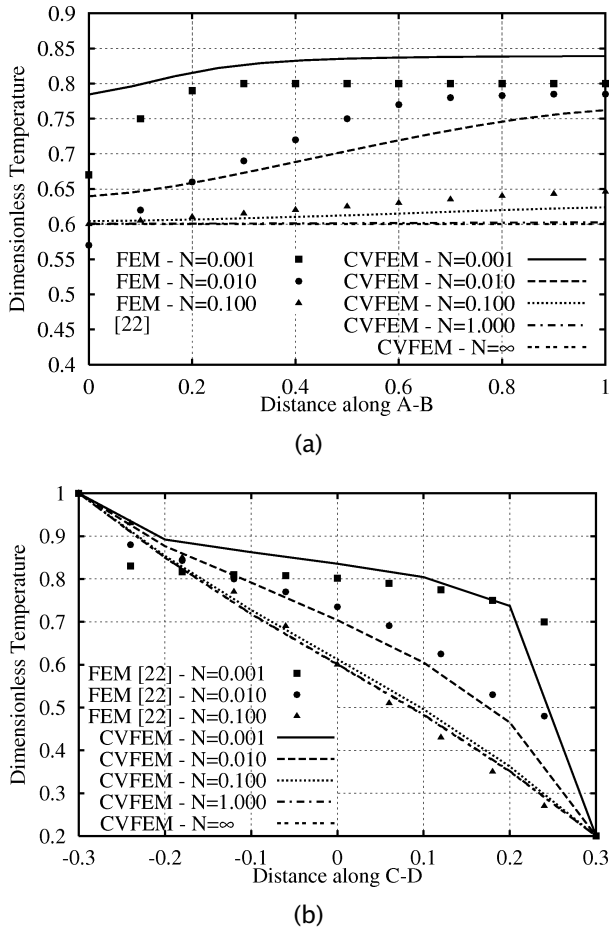

Figure 19. Conduction–convection–radiation in a divergent channel. Effect of Stark number, N, on: (a) centerline temperature; (b) cross-flow temperature at $x = L/2$. $\gamma = 0$, $\tau = 1$, $Pe = 100$.

If attention is directed towards the results presented for the middle cross-section *C-D* in *figure 17(b)*, it can be observed that the source term due to absorption raises the temperature profile above what was obtained for a scattering medium for the whole range of Peclet numbers investigated. Since radiation is 1 000 times more important than conduction, $N = 0.001$, the effect of the source term in the energy equation is more important for small *Pe*.

The effect of the scattering albedo variations is presented in *figure 18* for $\tau = 1$, $Pe = 100$, and $N = 0.001$. As the albedo increases for a constant τ, there is more and more scattering and proportionally less absorption. This causes the curves presented in *figure 18(a)* to approach the straight line $T/T_4 = 0.6$ as γ augments. Since $Bo = PeN/\tau = 0.1$, the influence of radiation with respect to that of convection is still 10 times more important. This is one of the reasons why the curve for $\gamma = 0.5$ is closer to that of $\gamma = 0$ than that of $\gamma = 1$. In *figure 18(b)*, it is shown that as the albedo increases, the curves naturally approach that of $\gamma = 1$.

In *figure 19*, the dimensionless centerline temperature and dimensionless cross-flow temperature at $x = L_x/2$ are presented for several values of N. Results are presented for an absorbing medium, $\gamma = 0$, with $\tau = 1$ and $Pe = 100$. It is shown that, as the importance of conduction over radiation increases for a fixed Peclet number, the centerline temperature profile along *A-B* approaches the purely scattering medium solution: that is $T/T_2 = 0.6$. When conduction dominates, $N > 1$, the source term in the energy equation has little effect because the Boltzmann number, *Bo*, becomes large. The solution for the midsection temperature profile clearly in-

TABLE V
Combined-modes of transfer in a divergent channel.
Number of iterations and CPU time.

Pe	Cond. Conv.		Cond. Conv. Rad.	
	Iter.	Time (s)	Iter.	Time (s)
1	2	0.20	30	11.32
100	2	0.33	26	10.85
1 000	2	0.58	15	8.99
10 000	2	1.66	7	5.83

dicates that when $N \to \infty$, the curve is nearly the one that is obtained in the case of pure convection–diffusion. When N is smaller, the energy absorbed by the media in the vicinity of the cold wall causes the temperature to increase along the axis.

When combined modes of heat transfer are simultaneously treated, CPU time and convergence rates become preponderant concerns. *Table V* indicates the number of iterations for the energy equation and CPU time needed to obtain a convergent solution for the case of conduction and convection only, and combined conduction, convection, and radiation. Similar discretizations for a purely absorbing medium of unit optical thickness and $N = 0.001$ were used. With $Pe = 1$, there is 1 000 times more heat transfer due to radiation than to convection and conduction. This explains why 30 iterations were needed for convergence of the algorithm: the source term in the energy equation was very large. As *Pe* augments, the relative importance of the divergence of the radiative flux (the source term) in the energy equation diminishes as well as the number of iterations needed for convergence. The CPU time ratio with and without radiation changes from 56 to 8 for $Pe = 1$ to $Pe = 10\,000$, respectively.

4.4. Conclusions regarding combined modes of heat transfer

The first problem permitted us to verify that the algorithms developed for conduction heat transfer and radiation heat transfer were compatible and that the same solver could indeed be used to solve for both phenomena.

The second problem was used to include the effects of convection in conjunction with radiation and conduction. Results provided confidence in both the formulation and implementation of the proposed method. The major conclusion that can be drawn from this second test problem is that radiation heat transfer has to be about 100 times more important than conduction heat transfer, $N = 0.01$, to introduce significant changes in the temperature distribution for a unit optical thickness, $\tau_0 = 1$.

The conclusions that can be drawn from the last test problem are that: (1) radiation heat transfer calculations can be carried out in a geometry that has boundaries unaligned with the axis of an orthogonal coordinate system; (2) radiation heat transfer has to be much more important than conduction and convection heat transfer (small *Bo*) to introduce significant changes in the temperature distribution for a unit optical thickness, $\tau_0 = 1$; (3) care must be provided to prescribe a flow field that satisfies continuity requirements everywhere in the calculation domain when the flow field is not calculated; (4) the convergence rate is slow for small values of the Stark number, as a small N implies a relatively important source term in the discretized energy equation.

It should be mentioned that when $\vec{\nabla} \cdot \vec{Q}_r$ is incorporated as a constant volumetric source term, S_C, in the A_P^* coefficient of the algebraic discretized energy equation, it can lead to very slow convergence of the iterative solution procedure, especially in radiation dominated situations. The solution may even diverge if $\tau_0 > 1$ and $N < 0.1$. To ensure convergence, it was found necessary to linearize appropriately the source term $\vec{\nabla} \cdot \vec{Q}_r$, and identify suitable S_C and S_P terms [4].

5. CONCLUSION

5.1. Contributions

In this paper, the capabilities of the CVFEMs proposed in [1] have been demonstrated by applying them to eleven test problems. Analytical closed-form solutions or independent numerical investigations available in the literature have been used to check the results produced by the CVFEM. These comparisons indicate that the CVFEM proposed by Rousse [1] can successfully solve combined-mode heat transfer problems in irregularly-shaped two-dimensional geometries filled with gray emitting, absorbing, and isotropically scattering media. Although this paper presents results limited to two-dimensional enclosures, the method used can be applied to three-dimensional geometries using tetrahedral elements.

5.2. Key features

Globally: (1) the solutions for combined-modes problems were found to be in good agreement with the few

reference solutions found in the literature. However, several combined-modes test problems should be proposed to become "benchmarks" problems; (2) the proposed method can solve combined-modes problems using the same assembly procedure for the coefficients of the algebraic discretization equations and the same solver for the three modes of transfer; (3) the computational time becomes very important with the increasing proportion of radiation heat transfer with respect to convection and conduction heat transfer.

In the context of convection–diffusion: (1) the skew positive coefficient upwind (SPCU) scheme produces positive coefficients in the algebraic discretization equations; (2) the SPCU scheme provides a reasonable level of accuracy but is prone to false diffusion. It gives better results when the longest side of a triangular element is nearly aligned with the average local flow field; (3) an Euler integration of ϕ combined with a linear velocity interpolation is adequate when the SPCU scheme is used; (4) the second-order flow-oriented (FLO) scheme produces solutions that are more accurate that those produced with the SPCU scheme, whenever the coefficients remain positive.

Concerning radiative transfer: (1) Since the CVFEM is a numerical solution of the exact governing equation, it should provide the exact solution within the limits of numerical accuracy and interpolation functions. Discretization refinement, both angular and spatial, is the key to obtain more accuracy. In most problems, coarse grids were found to yield accuracy levels that were satisfactory from an engineering point of view. (2) The low-order upwind scheme provides accurate solutions even for high optical thicknesses. This scheme was found to be the best compromise between accuracy of results and computer time requirements. (3) The computational time becomes important with increasing optical thickness and with decreasing wall emissivities.

5.3. Recommendations

During the testing of the proposed CVFEMs, it was noted that several improvements and extensions could be incorporated to increase the efficiency and scope for the solution of engineering problems. Among them: (1) the SPCU scheme for convection should be modified to include the physical additive correction (PAC) schemes such as that proposed by Galpin et al. [20]; with this modification, the effect of Peclet number and volumetric source terms could be explicitly included in the interpolation scheme; (2) adaptive grid techniques, based on grid redeployment and mesh enrichment strategies, should be explored and implemented; (3) fluid flow calculations should be incorporated; (4) capabilities to account for nongray media and boundaries should be investigated and a suitable model should be implemented; (5) problems involving anisotropically scattering media should be investigated; (6) nondiffuse or anisotropic reflection should be permitted; the concept of a reflection phase function should be investigated and tested; (7) strategies should be developed that allow for efficient assembly rules, and solution procedures on unstructured grids; (8) the approximations involved at the interpolation function level for the CVFEM for radiation heat transfer should be investigated and tested to determine the influence of such approximations on the accuracy and convergence rate of the method; (9) an implicit solution procedure such as that proposed by Chui [12], in the context of radiative equilibrium, should be elaborated and tested.

Acknowledgement

The authors gratefully acknowledge EDF for its support and the first author acknowledges the Natural Sciences and Engineering Research Council for an operating research grant.

REFERENCES

[1] Rousse D.R., Numerical predictions of two-dimensional conduction, convection, and radiation heat transfer. I. Formulation, Int. J. Therm. Sci. (2000) (to be published).

[2] Saabas H.J., A CVFEM for three-dimensional, incompressible, viscous fluid flow, PhD Thesis, McGill University, Montréal, 1991.

[3] Runchal A.K., Convergence and accuracy of three finite difference schemes for a two-dimensional conduction and convection problem, Internat. J. Numer. Meth. Engrg. 4 (4) (1972) 541–550.

[4] Patankar S.V., Numerical Heat Transfer and Fluid Flow, Hemisphere, Washington, 1980.

[5] LeDain-Muir B., Baliga B.R., Solution of three-dimensional convection–diffusion problems using tetrahedral elements and flow-oriented upwind interpolation functions, Numer. Heat Transfer 9 (1986) 143–162.

[6] Varejao L.M.C., Flux-spline method for heat, mass and momentum transfer, PhD Thesis, University of Minessota, Minneapolis, 1980.

[7] Rousse D.R., Numerical predictions of multidimensional conduction, convection, and radiation heat transfer in participating media, PhD Thesis, McGill University, Montréal, 1994.

[8] Fiveland W.A., Discrete-ordinates solutions of the radiative transport equation for rectangular enclosures, ASME J. Heat Tran. 106 (2) (1984) 699–706.

[9] Truelove J.S., Discrete-ordinate solutions of the radiation transport equation, ASME J. Heat Tran. 109 (4) (1987) 1048–1052.

[10] Modest M.F., Radiative equilibrium in a rectangular enclosure bounded by gray walls, J. Quant. Spectrosc. Radiat. Transfer 15 (1975) 445–461.

[11] Crosbie A.L., Schrenker P., Radiative transfer in a two-dimensional rectangular medium exposed to diffuse radiation, J. Quant. Spectrosc. Radiat. Transfer 31 (1984) 339–372.

[12] Chui E.H., Modelling of radiative heat transfer in participating media by the finite volume method, PhD Thesis, University of Waterloo, Canada, 1990.

[13] Chui E.H., Raithby G.D., Computation of radiant heat transfer on a non-orthogonal mesh using the finite volume method, Numer. Heat Transfer B 23 (1993) 269–288.

[14] Chai J.C., Lee H.S., Patankar S.V., Treatment of irregular geometries using a cartesian coordinates finite-volume radiation heat transfer procedure, Numer. Heat Transfer B 26 (1994) 225–235.

[15] Chai J.C., Parthasarathy G., Lee H.S., Patankar S.V., Finite-volume radiative heat transfer procedure for irregular geometries, J. Thermophys. Heat Transfer 9 (1995) 410–415.

[16] Liu J., Shang M., Chen Y.S., Prediction of radiative transfer in general body-fitted coordinates, Numer. Heat Transfer B 31 (1997) 423–439.

[17] Razzaque M.M., Howell J.R., Klein D.E., Finite element solution of heat transfer in a two-dimensional rectangular enclosure with gray participating media, ASME J. Heat Tran. 105 (4) (1983) 933–939.

[18] Viskanta R., Interaction of heat transfer by conduction, convection, and radiation in a radiating fluid, ASME J. Heat Tran. 85 (1963) 318–328.

[19] Chung T.J., Kim J.Y., Two-dimensional, combined-mode heat transfer by conduction, convection, and radiation in emitting, absorption, and scattering media-solution by finite elements, ASME J. Heat Tran. 106 (1984) 448–452.

[20] Galpin P.F., Huget R.G., Raithby G.D., Fluid flow simulations in complex geometries, in: CNS/ANS Second Int. Conf. on Simulation Methods in Nuclear Engineering, Montreal, 1986.